PHYSICAL REVIEW FLUIDS **9**, 074608 (2024)

Analysis of a turbulent round jet based on direct numerical simulation data at large box and high Reynolds number

Cat Tuong Nguyen and Martin Oberlack[*]
Technical University of Darmstadt, Chair of Fluid Dynamics
Otto-Bernd-Straße 2, 64287 Darmstadt, Germany

(Received 9 September 2023; accepted 20 May 2024; published 25 July 2024)

We have conducted a direct numerical simulation of a turbulent round jet at a previously unattained Reynolds number of $\mathrm{Re} = 3500$ based on the jet diameter D and jet-inlet bulk velocity U_b in a particularly long box of $75D$. To achieve very fast convergence to self-similarity, we used a turbulent pipe flow at the same Reynolds number and length $5D$ as the upstream inflow boundary condition. This indeed results in a very rapid emergence of self-similarity already at very small axial distances z compared to all turbulent jet data published so far. Not only for the mean velocities and the Reynolds stresses as well as the budgets of the Reynolds stress tensor and the turbulent kinetic energy, a nearly perfect classical scaling based on the normalized radius $\eta = r/z$ in the range $z/D = 25 - 65$ is shown, but also for the probability density function (PDF) of the axial velocity U_z as well as the associated skewness and kurtosis. All budget terms have been calculated directly, resulting in a marginal error in the balance. An almost completely Gaussian behavior of the PDF for the axial velocity is observed on the jet axis, while a clear deviation with increasingly heavy tails is evident with increasing distance from the axis.

DOI: 10.1103/PhysRevFluids.9.074608

I. INTRODUCTION

Round jet flows describe fluid flows ejected from a circular inlet into a semi-infinite domain. At a sufficiently high Reynolds number, this flow becomes turbulent, an important property that goes beyond academic curiosity. In aerospace engineering, turbulent jets play a critical role in jet propulsion systems, where understanding and optimizing jet dynamics is essential to improving engine performance and fuel efficiency. In addition, turbulent round jets serve as test beds for validating turbulence models and simulation techniques, providing benchmarks for assessing the accuracy and reliability of numerical predictions through its unique properties. In particular, turbulent round jet flows exhibit self-similarity in the far field, i.e., radial profiles of different statistical quantities can be scaled to converge to a single similarity function.

Universal self-similarity for turbulent round jets has long been discussed, where this state should be reached asymptotically and independent of initial conditions [1]. Yet, theoretical analysis shows that these self-similar profiles can depend on initial conditions [2]. Experimental results have indicated that, although a single jet is self-similar, the profiles differ in various experiments [3–5]. First assumptions have been inaccurate measurements due to disturbances by temperature

---

[*] Also at TU Darmstadt, Centre for Computational Engineering, Dolivostrasse 15, 64293 Darmstadt, Germany; Corresponding author: oberlack@fdy.tu-darmstadt.de

or uncontrollable turbulence in the ambient region which could be regulated by numerical simulations. However, since turbulent round jets grow in the axial direction, numerical simulations are computationally expensive.

Therefore, until the 1980s, the detailed statistical study of turbulent jet flows relied primarily on experimental methods. Wygnanski and Fiedler [3] conducted their experiment at a Reynolds number of Re = 100 000, where the Reynolds number was defined as

$$\mathrm{Re} = \frac{U_\mathrm{b} D}{\nu}, \tag{1}$$

with U_b, D, and ν being the inlet bulk velocity, inlet diameter, and kinematic viscosity, respectively. They took velocity measurements up to a normalized axial distance of $z/D = 100$ for first- to third-order statistics, highlighting a substantial disparity in the distance where self-similarity is attained, ranging from $z/D = 20$ for the first-order moment up to $z/D = 70$ for the second-order moment. This is explained with the energy, where self-similarity is reached in steps. First, the mean velocity reaches self-similarity, which amounts to a certain production of fluctuation which, in turn, allows the reach of equilibrium for the second-order moments. Considerably later, Panchapakesan and Lumley [4] conducted an experiment at Re = 11 000 taking velocity measurements in the range of $z/D = 30 - 150$, showing self-similarity up to fourth-order moments. In parallel, Hussein *et al.* [5] conducted their experiment at Re = 100 000, taking velocity measurements between $z/D = 50 - 122$, while the setup was based on Wygnanski and Fiedler [3]. Both groups were able to describe the turbulent kinetic energy balance but made different assumptions for the dissipation and pressure diffusion to close the turbulent kinetic energy (TKE) balance. Consequently, the results of both show disagreement due to these assumptions. Xu and Antonia [6] conducted an experiment measuring a jet exiting from a smooth contraction nozzle and from a pipe with a pipe flow profile at Re = 86 000, taking measurements in the range $z/D = 1 - 75$. They showed that a contraction jet reaches a state of self-preservation earlier than a fully developed pipe jet. This contrasts the experiments of Ferdman *et al.* [7], where they stated that a pipe jet reaches self-preservation earlier. However, both agree that for a fully developed pipe profile the far-field decay rate is smaller than in a top-hat velocity distribution, attributing it to a lack of potential core and surrounding mixing layer, which lead to a slower centerline mixing. Thus, the turbulence intensities on the centerline are smaller than those of a top-hat profile, according to Ferdman *et al.* [7]. Recently, Darisse *et al.* [8] collected results on a slightly heated round jet at Re = 140 000, where they also generated data on scalar quantities gathered at $z/D = 30$. They measured pure and mixed moments up to the third order, which allowed not only the determination of the turbulent kinetic energy balance, where, again, the pressure diffusion term was modeled and dissipation is found by closing the balance, but also the passive scalar transport balance, in which the dissipation is also calculated by closing the balance.

One of the early direct numerical simulations (DNSs) of a spatially developing turbulent round jet was by Boersma *et al.* [9]. They studied the effect of inflow conditions on the self-similarity scaling up to a box length of $z/D = 45$ at Re = 2400, showing that self-similarity is dependent on initial conditions. However, they were unable to resolve the far field due to limited computational resources, so the fluctuations did not yet fully reach self-similarity. Taub *et al.* [10] conducted a DNS at Re = 2000 at the same box length where they extracted statistics up to the third order, including the TKE terms and the terms of the Reynolds stress transport equations terms, directly. The data was extensively compared to previous studies. They also come to the conclusion that due to different approximations in previous experimental studies, there have been inconsistencies in the dissipation profiles and which may also be due to the Reynolds number dependence of the dissipation [11]. Later, Shin *et al.* [12] found self-similarity in a DNS at Re = 7290 after $z/D = 15$ for the first and after $z/D = 25$ for the second moment in a box length of $z/D = 60$. Only in their study, the profiles of the moments of second order were shown at various distances z but the collapse is rather unsatisfactory since the statistics have only been taken over $80D/U_\mathrm{b}$ units. They showed that moments up to the fourth order and the one-point probability density function (PDF) of

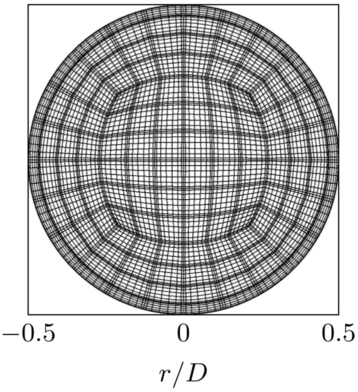

FIG. 1. Cross-sectional view of the computational domain for the pipe. The $N = 7$ GLL points has been included in the mesh.

mass-weighted stream-age, the product of the jet fluid residence time, and the jet fluid mass fraction are self-similar.

Currently, we present high quality statistics of a round jet DNS at a comparably large Re, a long box of $z/D = 75$, and statistics taken over $75\,000 D/U_\mathrm{b}$ time units where the velocity profile of a turbulent pipe flow is utilized as an inlet. The statistics are compared to the aforementioned studies and the collapse at various distances from the orifice are shown, which most studies omit. Also, the TKE budget terms are calculated directly from the simulation and the PDF of the axial velocity is discussed.

II. NUMERICAL METHOD

Presently, we employ the Navier-Stokes equations (NSEs) for an incompressible fluid consisting of the continuity equation

$$\nabla \cdot \boldsymbol{U} = 0 \tag{2}$$

and the momentum balance equations

$$\frac{\partial \boldsymbol{U}}{\partial t} + (\boldsymbol{U} \cdot \nabla)\boldsymbol{U} = -\nabla P + \frac{1}{\mathrm{Re}}\nabla^2 \boldsymbol{U}, \tag{3}$$

with $\boldsymbol{U}, P, t$ being the nondimensionalized velocity vector, pressure, time, and the Reynolds number Re defined in (1).

The NSEs (2) and (3) are solved numerically using NEK5000 developed by Fischer [13], and which is based on a high order spectral element method (SEM) (see, e.g., [Ref. [14]]). NEK5000 has a highly efficient parallel implementation and for optimal efficiency the polynomial order $N = 7$ and the BDF2 scheme has been used for time stepping.

We presently adopt a fully developed turbulent pipe flow as an inlet condition, since this leads to self-similarity occurring closer to the inlet. For this, the computational domain has been split into two domains, i.e., a periodic pipe flow to generate the inlet condition and the main computational domain to capture the turbulent jet flow. A bulk Reynolds number of $\mathrm{Re} = 3500$ has been chosen since it lies in the range of a fully turbulent pipe flow and still is computationally feasible with the available computational resources.

The computational domain for the pipe in radial and axial directions is $0.5D \times 5D$ with 132 and 30 cells in the r, φ plane (see Fig. 1) and z direction, respectively, and with the usual refinement towards the near-wall region. Factoring in the $N = 7$ Gauss-Lobatto-Legendre (GLL) points, the pipe mesh has around 5 400 000 grid points. The boundary conditions at the wall are no-slip and impermeable wall while at $z = -5D$ and $z = 0$ periodicity has been employed. To generate

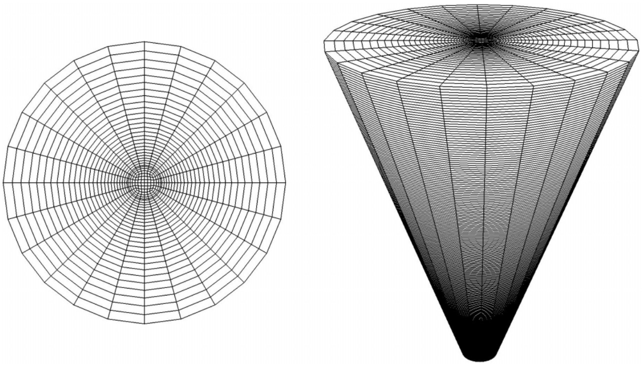

FIG. 2. Cross-sectional view of the main computational box at $z/D = 0$ (left) which is scaled linearly in z direction to obtain the whole main computational box (right). The GLL points are omitted for better visibility.

a turbulent flow field in the pipe, a small disturbance in all three directions is superposed to the initially laminar pipe flow profile $U_z = 6/D^2(1/4 - r^2)$. Pressure gradient and viscosity are set, such that the bulk velocity is 1 and $\mathrm{Re} = 3500$. After running the simulation until a fully developed turbulent pipe flow has been reached, the velocities at the cross section $z = 0$ are interpolated onto the inlet of the computational domain of the jet flow at each time step.

The main computational box of the jet DNS at the inlet $z/D = 0$ is $4D$ and at the outlet $z/D = 75$ is $64D$ to investigate the near and far-field behavior of self-preservation (see Fig. 2). This ensures capturing the spreading of the jet and to prevent interactions with the lateral far-field boundaries to ensure high-quality statistics. The boundary condition at $z/D = 0$ outside of the jet inlet has been set as a no-slip wall while the lateral boundaries and the jet exit at $z/D = 75$ have been configured as open boundaries following the approach introduced by Dong *et al.* [15]. This open boundary is designed to locally prevent the kinetic energy influx into the domain at the outflows, addressing a key challenge in DNS of jet flows that leads to instabilities. This is achieved by balancing the energy influx with the effective stress. Otherwise, it functions as a standard open outflow boundary condition with zero pressure, thereby enabling entrainment. Additionally, special attention was paid to obtaining very accurate statistics, and for all moments shown below, averages were taken over $75\,000 D/U_b$ times. Despite the significantly larger box, this corresponds to nearly 200 passes of a particle through the entire computational domain of the jet and is a factor of 25 longer than the largest simulations to date. The computational mesh consists of an inner pipe-type mesh and an outer conical mesh. Both are scaled linearly in the radial direction when moving axially. In the axial direction, the cells of both the pipe and the outer part are stretched geometrically with the factor of 1.006 with 234 cells. Around the inner part, the cells are stretched geometrically in the transverse direction with the factor of 1.06 with 25 cells. Considering the $N = 7$ GLL points, the main computational mesh has around 180 000 cells, which amounts to 240 000 000 degrees of freedom. All simulations were performed on the GCS supercomputer SUPERMUC-NG at Leibniz Supercomputing Centre, Garching, Germany, using a total of 24 000 000 CPUh and around 25 000 cores in parallel. Figure 3 shows a snapshot of isosurfaces of the q criterion [16], a quantity used to capture vortices, at $q = 0.01$. It can be observed that the transition to turbulence and therefore the spreading of the jet occurs close to the orifice compared to earlier studies (see Fig. 4), resulting in $z_0 = 0$ in (4) below.

III. ONE-POINT STATISTICS

Classically, the mean velocities of a self-preserving jet are scaled with the centerline velocity [9]

$$\frac{\overline{U}_{z,c}(z)}{\overline{U}_0} = \frac{B_u D}{z - z_0}, \tag{4}$$

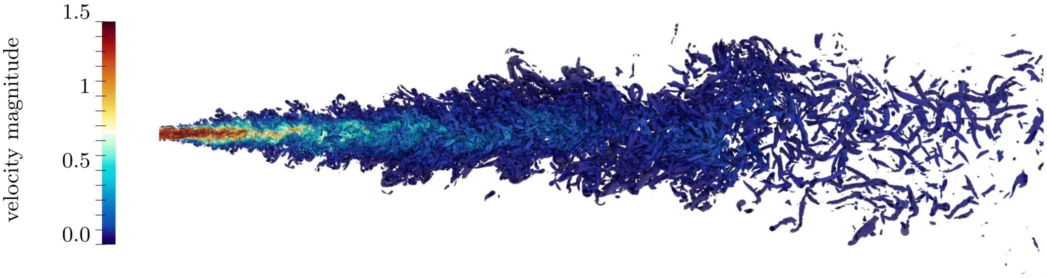

FIG. 3. A cross section of q-criterion isosurfaces at $q = 0.01$ of the conducted jet DNS colored with the velocity magnitude.

where $\overline{U}_0 = 1.38$ refers to the mean axial centerline velocity at the orifice, B_u to the decay constant, and z_0 to the virtual origin. In Fig. 4, the inverse of the mean axial centerline velocity according to (4) is compared to other DNS and experimental data. Presently, the Reynolds decomposition $\boldsymbol{U} = \overline{\boldsymbol{U}} + \boldsymbol{u}$ is adopted, with $\overline{\boldsymbol{U}}$ and $\boldsymbol{u}$, respectively, the mean velocity and the fluctuations. Values for the present DNS and other works are given in Table I. The present values for the parameters have been determined by minimizing the sum of the squares of the residuals relative to the DNS data on the conservative interval $z/D = 15 - 65$. We purposely do not include the last part of the box due to boundary effects. Nevertheless, the average relative residual on the interval $z/D = 15 - 75$ is 0.2%. The decay rate B_u of the present DNS is slightly lower compared to previous results, while the virtual origin z_0 is zero, which may be due to early mixing caused by our fully turbulent inlet. In classical jet theory, the radial coordinate is nondimensionalized with

$$\eta = \frac{r}{z - z_0}. \tag{5}$$

For the jet half-width $\eta_{1/2}$, we find $\eta_{1/2} = 0.089$ (see Fig. 5), and which is in the range of what has been observed previously to be taken from Table I. The differences are due to the different inlet conditions. In Fig. 6, the mean radial velocity $\overline{U}_r/\overline{U}_{z,c}$ reaches a maximum outward velocity of $\overline{U}_{r,\max}/\overline{U}_{z,c} = 0.017$ at $\eta = 0.056$, while the maximum inward velocity is at $\eta = 0.22$ with $\overline{U}_{r,\min}/\overline{U}_{z,c} = -0.022$. The values of $\overline{U}_r$ on the centerline and of $\overline{U}_\varphi$ in the whole domain are very small and in the order of 10^{-4}. Figures 5 and 6 show an excellent collapse of the DNS data according to the classical scaling

$$\overline{U}_i(r, z) = \frac{\tilde{\overline{U}}_i(\eta)}{(z - z_0)} \tag{6}$$

for the mean velocity in the range $z/D = 25 - 65$, where $\tilde{\overline{U}}_i(\eta)$ refers to the invariant or similarity variable, i.e., the collapsed profiles only dependent of η. Subsequently, this is also observed for velocity moments up to $n = 10$. Furthermore, Fig. 7 showcases the invariant $\tilde{\overline{U}}_z(\eta = 0) = B_u D \overline{U}_0$

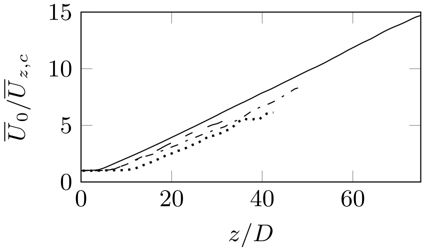

FIG. 4. Inverse of the mean axial centerline velocity according to Eq. (4) plotted over the distance from the orifice. Present DNS (——), Boersma [9] (······), Babu [17] (· - - -), Taub [10] (- —).

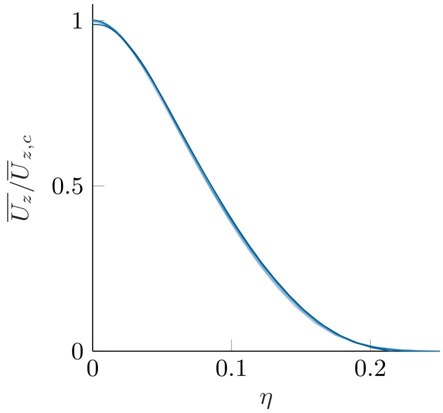

FIG. 5. Mean axial velocity profiles normalized with the axial centerline velocity according to Eq. (6) as functions of η at different distances from the orifice: $z/D = 25$ (——), 35 (——), 45 (——), 55 (——), 65 (——).

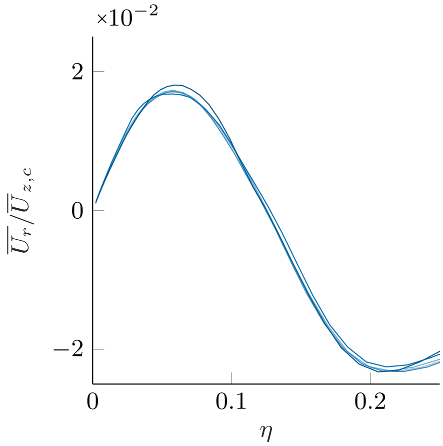

FIG. 6. Mean radial velocity profiles normalized with the axial centerline velocity according to Eq. (6) as functions of η at different distances from the orifice: $z/D = 25$ (——), 35 (——), 45 (——), 55 (——), 65 (——).

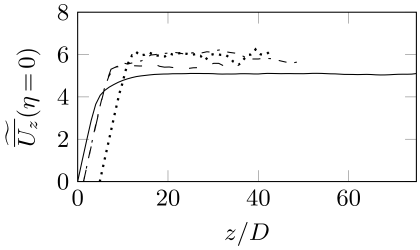

FIG. 7. The invariant $\widetilde{\overline{U}_z}(\eta = 0)$ plotted over the distance from the orifice. Present DNS (——), Boersma [9] (······), Babu [17] (· - · -), Taub [10] (- —).

TABLE I. Various jet parameters of DNS and experiments.

Reference	Re	B_u	z_0	$\eta_{1/2}$
Wygnanski [3]	10^5	5.7	3.0	0.085
Panchapakesan [4]	1.1×10^4	6.06	0.0	0.096
Hussein [5]	10^5	5.8	4.0	0.094
Boersma [9]	2400	5.9	4.9	0.091
Taub [10]	2000	5.4	1.3	0.096
Present DNS	3500	5.15	0.0	0.089

according to (6) being valid in the far field, which further supports the $1/z$ decay depicted in Fig. 4. It can be observed that the statistics of the present DNS are very well converged up to the end of the domain compared to previous studies. The lower value compared to the other studies is due to the lower decay rate B_u.

Figures 8 and 9 compare the components of the turbulence intensity on the centerline with the DNS from Taub *et al.* [10], large eddy simulation (LES) from Bogey and Bailly [18], and an experiment from Panchapakesan and Lumley [4]. In Fig. 8, a fast increase of the radial component of the turbulence intensity is observed starting at $z/D = 70$, which is due to the boundary effects which we have tried to counteract by employing the outflow boundary condition by Dong *et al.* [15], preventing an uncontrolled growth in the energy imposed by the boundary. This increase is transported by the large eddies from the boundary into the domain at the end of the box. This effect, if ever so slightly, can also be observed in Fig. 7 close to $z/D = 75$. In Fig. 9, this effect does not become apparent, although it can be assumed that it does marginally.

In Taub *et al.* [10], it is mentioned that both in theirs and in the study of Bogey and Bailly [18], an almost constant value is reached after the transition region and that experiments reach an asymptotic value gradually. This seems, however, only a first approximation, as the variance in the turbulence intensity of the study by Taub *et al.* [10] is still quite high and the LES by Bogey and Bailly [18] only covers a small axial distance.

There are mainly two methods to shorten the transition region, the first being a smaller Re [18] and the second being a faster initiation of the turbulent behavior. The incline of the present DNS in Fig. 7 starts at $z/D = 0$ compared to other DNS studies showing that the transition begins earlier. However, it is not apparent that a constant value is achieved earlier, which might be due to the higher Re of the present DNS at Re = 3500 compared to other studies where the range is Re = 2000 − 2400. Additionally, in Figs. 8 and 9, we observe a nonzero turbulence intensity at $z/D = 0$ which has not been achieved by the other studies shown in those figures. Taub *et al.* [10] superimposed small nonphysical perturbations onto a top-hat profile while Bogey and Bailly [18] used divergence-free vortex rings near the inlet. We conclude that using a turbulent velocity

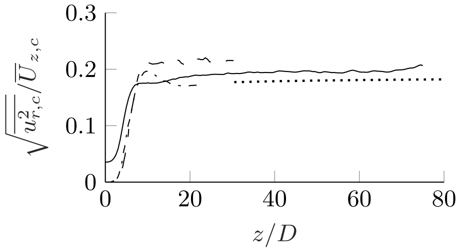

FIG. 8. Radial component of the turbulence intensity on the centerline compared to previous studies: Present DNS (——), Taub [10] (‐ ‐), Bogey [18] (· ‐ · ‐), Panchapakesan [4] (······).

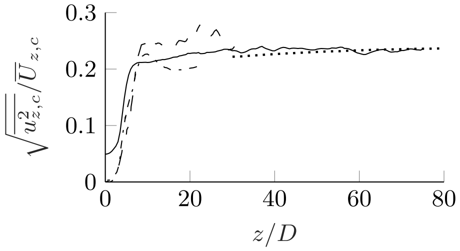

FIG. 9. Axial component of the turbulence intensity on the centerline compared to previous studies: Present DNS (——), Taub [10] (– —), Bogey [18] (· – · –), Panchapakesan [4] (······).

profile may shorten the transition region. However, a study to confirm this by comparing different inlet conditions at a constant Re would be beneficial. The DNS in Taub *et al.* [10], where random perturbations have been introduced on the axial velocity profile, seems therefore not sufficient to initiate fully turbulent behavior. The far-field behavior of the present DNS is closer to the experimental study by Panchapakesan and Lumley [4] as the turbulence intensities slowly increases.

According to the classical scaling, all Reynolds stresses of the present DNS are scaled with $\overline{U}^2_{z,c}$, i.e.,

$$\overline{u_i u_j}(r, z) = \frac{\widetilde{\overline{u_i u_j}}(\eta)}{(z - z_0)^2}, \tag{7}$$

and are shown in Fig. 10, where $\widetilde{\overline{u_i u_j}}(\eta)$ refers to the invariant or similarity variable in accord with Eq. (6). The profiles are presented for different axial distances from the orifice exhibiting an excellent collapse. As mentioned by previous works [4,5,10], the off-center maxima are due to the strong interaction of the jet with the ambient fluid in that region.

IV. TURBULENT BUDGETS

The budget equations of the Reynolds stresses read

$$C_{ij} + \Pi_{ij} + P_{ij} + T_{ij} + \varepsilon_{ij} + V_{ij} = 0, \tag{8}$$

see, e.g., Refs. [19,20], with $i, j = r, \varphi, z$, where, from the right, the terms, respectively, denote convection, velocity-pressure gradient correlation, production, turbulent diffusion, dissipation, and viscous diffusion. Due to the statistical axisymmetry of the flow, all terms $(\cdot)_{\varphi z}$ and $(\cdot)_{r\varphi}$ are zero and the same holds for the unsteady term. Further, the viscous diffusion is negligible due to a high Reynolds number [10]. The five nonzero transport equations are shown in (9)–(12), while

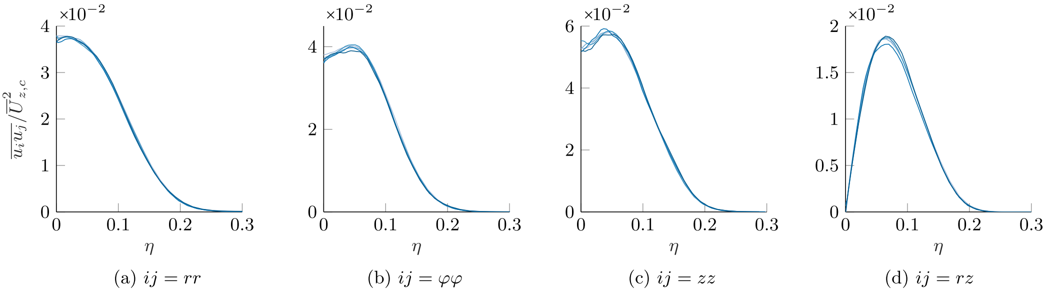

(a) $ij = rr$ (b) $ij = \varphi\varphi$ (c) $ij = zz$ (d) $ij = rz$

FIG. 10. Reynolds stresses $\overline{u_i u_j}$ normalized with the axial centerline velocity $\overline{U}^2_{z,c}$ according to Eq. (7) at different distances from the orifice: $z/D = 25$ (——), 35 (——), 45 (——), 55 (——), 65 (——).

the brackets refer to the terms in Eq. (8), respectively, where the viscous term has already been neglected as the DNS also shows that the term is close to zero: $\overline{u_r u_r}$ transport equation:

$$\begin{aligned} 0 = &-\left[\overline{U}_z \frac{\partial}{\partial z}\overline{u_r u_r} + \overline{U}_r \frac{\partial}{\partial r}\overline{u_r u_r}\right] - \left[2\overline{u_r \frac{\partial p}{\partial r}}\right] - \left[2\overline{u_r u_r}\frac{\partial \overline{U}_r}{\partial r} + 2\overline{u_z u_r}\frac{\partial \overline{U}_r}{\partial z}\right] \\ &-\left[\frac{\partial \overline{u_z u_r^2}}{\partial z} + \frac{1}{r}\frac{\partial}{\partial r}\left(r\overline{u_r^3}\right) - 2\frac{\overline{u_r u_\varphi^2}}{r}\right] - \frac{2}{\mathrm{Re}}\left[\overline{\left(\frac{\partial u_r}{\partial z}\right)^2} + \overline{\left(\frac{\partial u_r}{\partial r}\right)^2} + \frac{1}{r^2}\overline{\left(\frac{\partial u_r}{\partial \varphi}\right)^2}\right]; \end{aligned} \tag{9}$$

$\overline{u_\varphi u_\varphi}$ transport equation:

$$\begin{aligned} 0 = &-\left[\overline{U}_z \frac{\partial}{\partial z}\overline{u_\varphi u_\varphi} + \overline{U}_r \frac{\partial}{\partial r}\overline{u_\varphi u_\varphi}\right] - \left[2\overline{\frac{u_\varphi}{r}\frac{\partial p}{\partial \varphi}}\right] - \left[2\frac{\overline{U}_r}{r}\overline{u_\varphi u_\varphi}\right] \\ &-\left[\frac{\partial \overline{u_z u_\varphi^2}}{\partial z} + \frac{1}{r}\frac{\partial}{\partial r}\left(r\overline{u_r u_\varphi^2}\right) + 2\frac{\overline{u_r u_\varphi^2}}{r}\right] - \frac{2}{\mathrm{Re}}\left[\overline{\left(\frac{\partial u_\varphi}{\partial z}\right)^2} + \overline{\left(\frac{\partial u_\varphi}{\partial r}\right)^2} + \frac{1}{r^2}\overline{\left(\frac{\partial u_\varphi}{\partial \varphi}\right)^2}\right]; \end{aligned} \tag{10}$$

$\overline{u_z u_z}$ transport equation:

$$\begin{aligned} 0 = &-\left[\overline{U}_z \frac{\partial}{\partial z}\overline{u_z u_z} + \overline{U}_r \frac{\partial}{\partial r}\overline{u_z u_z}\right] - \left[2\overline{u_z \frac{\partial p}{\partial z}}\right] - \left[2\overline{u_z u_z}\frac{\partial \overline{U}_z}{\partial z} + 2\overline{u_z u_r}\frac{\partial \overline{U}_z}{\partial r}\right] \\ &-\left[\frac{\partial \overline{u_z^3}}{\partial z} + \frac{1}{r}\frac{\partial}{\partial r}\left(r\overline{u_z^2 u_r}\right)\right] - \frac{2}{\mathrm{Re}}\left[\overline{\left(\frac{\partial u_z}{\partial z}\right)^2} + \overline{\left(\frac{\partial u_z}{\partial r}\right)^2} + \frac{1}{r^2}\overline{\left(\frac{\partial u_z}{\partial \varphi}\right)^2}\right]; \end{aligned} \tag{11}$$

$\overline{u_r u_z}$ transport equation:

$$\begin{aligned} 0 = &-\left[\overline{U}_z \frac{\partial}{\partial z}\overline{u_r u_z} + \overline{U}_r \frac{\partial}{\partial r}\overline{u_r u_z}\right] - \left[\overline{u_r \frac{\partial p}{\partial z}} + \overline{u_z \frac{\partial p}{\partial r}}\right] \\ &-\left[\overline{u_r u_z}\frac{\partial \overline{U}_z}{\partial z} + \overline{u_r u_r}\frac{\partial \overline{U}_z}{\partial r} + \overline{u_z u_z}\frac{\partial \overline{U}_r}{\partial z} + \overline{u_r u_z}\frac{\partial \overline{U}_r}{\partial r}\right] \\ &-\left[\frac{\partial \overline{u_z^2 u_r}}{\partial z} + \frac{1}{r}\frac{\partial}{\partial r}\left(r\overline{u_z u_r^2}\right) - \frac{\overline{u_z u_\varphi^2}}{r}\right] - \frac{2}{\mathrm{Re}}\left[\overline{\frac{\partial u_r}{\partial z}\frac{\partial u_z}{\partial z}} + \overline{\frac{\partial u_r}{\partial r}\frac{\partial u_z}{\partial r}} + \frac{1}{r^2}\overline{\frac{\partial u_r}{\partial \varphi}\frac{\partial u_z}{\partial \varphi}}\right]. \end{aligned} \tag{12}$$

The velocity-pressure gradient correlation term offers more information when split into a pressure diffusion and pressure strain term $\Pi_{ij} = \Pi_{ij}^d - \Pi_{ij}^s$. The terms on the right side in brackets in (13) correspond to pressure diffusion and pressure strain, respectively:

$$\begin{aligned} 2\overline{u_r \frac{\partial p}{\partial r}} &= \left[2\frac{\partial}{\partial r}\overline{p u_r}\right] - \left[2\overline{p\frac{\partial u_r}{\partial r}}\right], \\ \overline{\frac{2}{r}u_\varphi \frac{\partial p}{\partial \varphi}} &= \left[\frac{2}{r}\frac{\partial}{\partial \varphi}\overline{p u_\varphi}\right] - \left[\overline{\frac{2}{r}p\frac{\partial u_\varphi}{\partial \varphi}}\right], \\ 2\overline{u_z \frac{\partial p}{\partial z}} &= \left[2\frac{\partial}{\partial z}\overline{p u_z}\right] - \left[2\overline{p\frac{\partial u_z}{\partial z}}\right], \\ \overline{u_r \frac{\partial p}{\partial z}} + \overline{u_z \frac{\partial p}{\partial r}} &= \left[\frac{\partial}{\partial z}\overline{p u_r} + \frac{\partial}{\partial r}\overline{p u_z}\right] - \left[\overline{p\frac{\partial u_r}{\partial z}} + \overline{p\frac{\partial u_z}{\partial r}}\right]. \end{aligned} \tag{13}$$

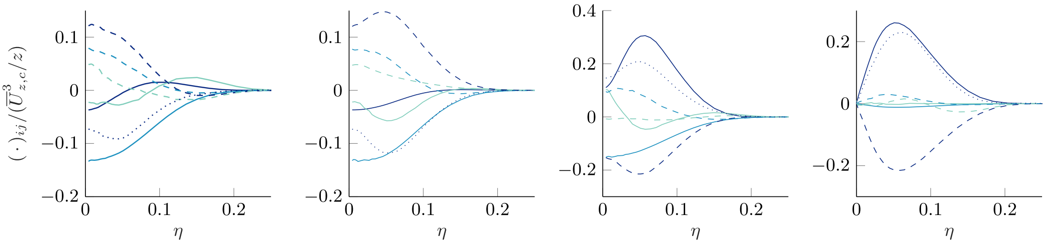

(a) $ij = rr$ (b) $ij = \varphi\varphi$ (c) $ij = zz$ (d) $ij = rz$

FIG. 11. Budgets of the Reynolds stresses scaled with $\overline{U}^3_{z,c}/z$ at $z/D = 25$: production (——), dissipation (——), turbulent diffusion (——), velocity-pressure gradient correlation (- - -), convection (- - -), pressure diffusion (- - -), pressure strain (⋯⋯).

Each term in (8), i.e., the four transport equations (9)–(12) scale as

$$\tilde{E}_{ij} = \frac{E_{ij} z}{\overline{U}^3_{c,z}}, \tag{14}$$

where E_{ij} defines any tensor in (8). All terms evaluated employing the present DNS data can be viewed in Fig. 11. The terms have all been calculated in Cartesian coordinates which were then transformed to its cylindrical form and have been averaged in the azimuthal direction, subsequently. In Fig. 11, quite deliberately only the curves for $z/D = 25$ are shown, although budgets also possess an excellent self-similarity. The background is that, as visible in Fig. 10, for the second moments of the fluctuations weak deviations near the jet axis are observed despite the presently conducted extensive statistics. The abundance of curves would make Fig. 11 less readable.

From (8), we derived the equation for the TKE $k = 1/2\,\overline{u_i u_i}$:

$$C^k + \Pi^{k,d} + P^k + T^k + \varepsilon^k + V^k = 0. \tag{15}$$

The TKE budget terms and their sum are shown in Fig. 12 and, for the same reasons as for the budgets of the Reynolds stresses, here too we focus only on values at $z/D = 25$. All terms have been again calculated directly from the DNS according to (14). The sum of the budget terms, i.e., the error in the TKE balance, is below 0.0126 and corresponds to 6% error compared to the maximum value of the dissipation for all values of η in the same scaling as in Fig. 12, which is contrasted to the

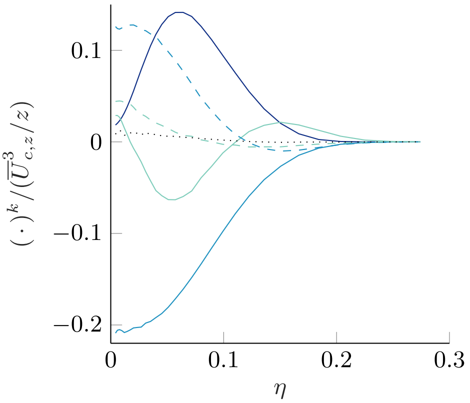

FIG. 12. Turbulent kinetic energy budgets at $z/D = 25$: production (——), dissipation (——), turbulent diffusion (——), convection (- - -), pressure diffusion (- - -), sum of the budget terms (⋯⋯).

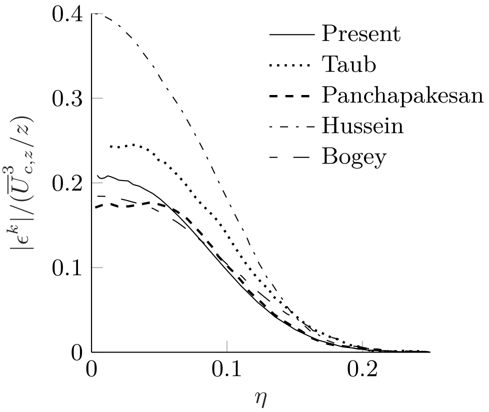

FIG. 13. The dissipation of the turbulent kinetic energy comparing the present DNS at Re = 3500 to the DNS of Taub *et al.* [10] at Re = 2000, the experiments of Panchapakesan and Lumley [4] at Re = 11 000, Hussein *et al.* [5] at Re = 100 000, and a LES of Bogey and Bailly [18] at Re = 11 000.

error of 0.02 in the DNS of Taub *et al.* [10]. The viscous diffusion is close to zero and is therefore not included in the figure.

The Kolmogorov length scale is $\eta_K = (\nu^3/\epsilon)^{1/4} = 0.0012z$, where the dissipation ϵ has been taken from Fig. 12 and dissipation scales as (14). We can see, e.g., for $z = 25D$ the Kolmogorov length scale is $\eta_K = 0.03D$ and the grid spacing on the centerline is Δx, $\Delta y = 0.061D$ while at $z = 65D$, $\eta_K = 0.078D$, and Δx, $\Delta y = 0.14D$. The criterion for a good resolution of the smallest scales is $\Delta x/\eta = 2.1$ [21], which we satisfy here for the entire domain.

The dissipation on the centerline is about twice as large as the convection term. This agrees with Hussein *et al.* [5], Wygnanski and Fiedler [3], and Darisse *et al.* [8], whereas Panchapakesan and Lumley [4] and Taub *et al.* [10] found that the values are about the same. In some works [10,11], it is speculated that this might be due to the difference in Reynolds number even for high Reynolds numbers. However, the magnitude of the Reynolds number of the present DNS is closer to the latter mentioned studies (see Table I). Since the studies above used top-hat profiles as the inlet condition, this could mean that the fully turbulent velocity profile at the inlet of the present DNS influences the dissipation similarly to a higher Re. Further, in Fig. 13, the dissipation of the present DNS is compared to some of these studies where the dissipation has a similar profile but reaches different magnitudes. Only the studies of Taub *et al.* [10], Bogey and Bailly [18], and the present paper have calculated the dissipation directly, while Hussein *et al.* [5] approximated the dissipation by assuming local isotropy. Taub *et al.* [10] also calculated the dissipation using the approximation by Hussein *et al.* [5] where the dissipation has been overestimated. It is important to note that Taub *et al.* [10] used a second-order finite volume scheme which yields different results than the high-order scheme employed in this paper [22,23]. Also, Bogey and Bailly [18] conducted a LES, which in itself already contains models. The dissipation of the present DNS is clearly very similar to the studies of Panchapakesan and Lumley [4] and Bogey and Bailly [18], both at Re = 11 000, which further supports this assumption of a turbulent inlet influencing the dissipation, similar to a higher Re.

The previous results may now be used to evaluate Kolmogorov‘s relation

$$\epsilon = C_\epsilon \frac{k^{\frac{2}{3}}}{l}, \tag{16}$$

where l is the integral length scale $l = \frac{1}{4\pi k} \iiint \frac{R_{mm}(\boldsymbol{r})}{|\boldsymbol{r}|^2} \mathrm{d}^3 r$, $R_{mm}(\boldsymbol{r})$ is the two-point correlation, and $\boldsymbol{r}$ the distance between two points. Implementing (7) and (14) into Kolmogorov‘s relation (16), where we extended (7) to two-point correlations, we find that z drops out on both sides and hence C_ϵ does not depend on the local Reynolds number as was found for certain other flows [24].

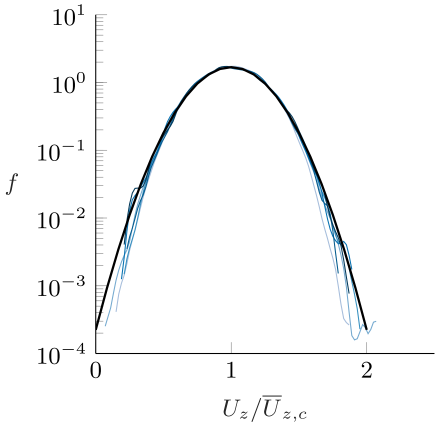

FIG. 14. PDFs of $U_z(\eta = 0, z)/\overline{U}_{z,c}(z)$ at $z/D = 15$ (——), 25 (——), 35 (——), 45 (——), 55 (——), 65 (——) compared to a Gaussian (——).

V. PROBABILITY DENSITY FUNCTIONS

In addition to the classical variables of mean velocity, Reynolds stresses, and budgets, extensive DNS statistics enabled us to compute higher-order statistics, i.e., PDFs, at high precision. We created the PDFs by collecting U_z at various points every $0.05D/U_\mathrm{b}$ over the time span of $75\,000D/U_\mathrm{b}$. The data is then divided in bins where data of a given r and z can be collected in the same PDF, which contributed to the smoothness of the resulting PDFs. After binning the data, we calculated the density of occurrence for each bin. This involved counting the number of data points falling within each bin. To ensure that our PDFs represented true probabilities, we normalized these densities so they summed up to 1.

In Fig. 14, the PDF f of the normalized axial centerline velocity also shows an excellent collapse for different distances z/D from the orifice. On the centerline, the PDF f are well described by a Gauss distribution. Additionally, the PDF development at $z/D = 28, 42, 56$ for varying η is shown in Fig. 15. It can be clearly seen that for increasing η, the curves slowly deviate from a Gaussian, and non-Gaussian tails develop. By further increasing η, a delta distribution is approached due to a laminar constant ambiance velocity. Most important, we observe an excellent PDF data collapse due to the η scaling. Further and also theoretical analysis of the PDF are ongoing and will be presented in a later publication.

Finally, in Fig. 16 the U_z-based skewness S and kurtosis K is extracted from the data. Also, these values show an almost perfect collapse in the range of similarity. A skewness of $S = 0$ and kurtosis of $K = 3$ correspond to characteristics of a Gaussian distribution. This indicates that on the

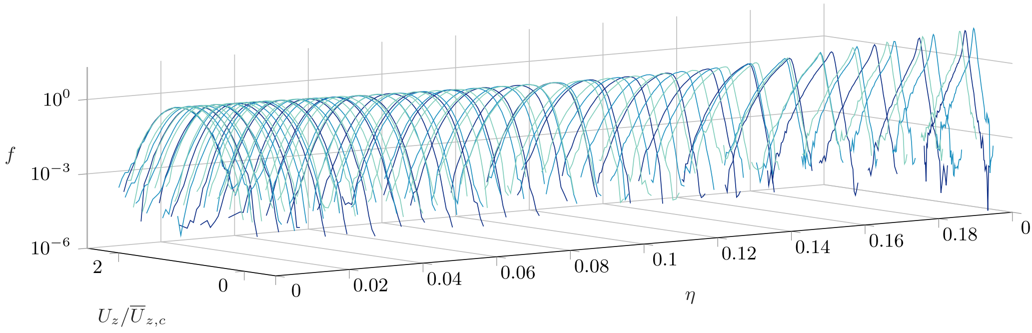

FIG. 15. PDFs of $U_z(\eta, z)/\overline{U}_{z,c}(z)$ for $z/D = 28$ (——), 42 (——), 56 (——).

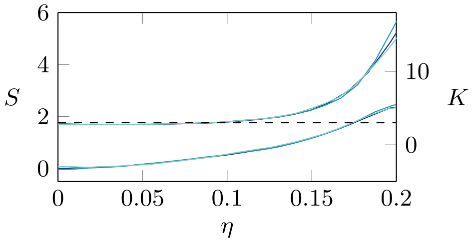

FIG. 16. Kurtosis K (above) and skewness S (below) of $U_z(\eta, z)/\overline{U}_{z,c}(z)$ for $z/D = 28$ (——), 42 (——), 56 (——). $K = 3$ (dashed), $S = 0$ are the Gaussian values.

jet centerline $\eta = 0$, the PDFs closely resemble a Gaussian distribution. As η increases, the PDFs show increasing positive skewness with $K = 3$ until $\eta = 0.09$. Beyond this point, the PDFs deviate from Gaussian behavior, becoming increasingly non-Gaussian as they eventually approach a delta distribution in the laminar region of the flow very far away from the jet axis.

VI. CONCLUSION

In conclusion, a turbulent round jet flow at Re $= 3500$ has been simulated. The size of the box extends up to $75D$ in the axial and up to $65D$ in the radial direction to ensure the caption of the far-field statistics. The statistics are taken over $75\,000D/U_b$ units, which corresponds to 200 passes of a particle through the domain. High-quality statistics have been generated for the velocity statistics of first- and second-order one-point moments. Furthermore, all the terms of the Reynolds stress equations and the turbulent kinetic energy equation have been generated directly from the DNS data. Additionally, for the axial velocity, PDFs have been generated in the radial and axial directions, which to the authors' knowledge has not been reported in literature before. The mean axial centerline velocity shows a highly converged $1/z$ behavior up to the end of the box. All the radial velocity profiles of the first- and second-order statistics show a remarkable collapse based on classical scaling. The turbulence intensities show a slight axial increase similar to experimental studies, which could not be shown by DNS conducted before as the boxes have been too small. Further, a fully turbulent velocity profile as an inlet might have similar effects on the dissipation as an increase in Re.

The database containing the data shown can be downloaded from the TUdatalib Repository of TU Darmstadt at Ref. [25].

ACKNOWLEDGMENTS

The authors gratefully acknowledge the Gauss Centre for Supercomputing e.V. [26] for funding this project under Project No. pn73fu by providing computing time on the GCS Supercomputer SUPERMUC-NG at Leibniz Supercomputing Centre [27]. The authors also thank S. Hoyas for his helpful insights and P. Schlatter for his kind guidance on the modification of the NEK5000 toolbox [28] for computing turbulence statistics. Further, C.T.N. acknowledges funding from the Studienstiftung des deutschen Volkes (Academic Scholarship Foundation) and M.O. gratefully acknowledges partial funding by the Deutsche Forschungsgemeinschaft (DFG, German Research Foundation)—SPP 2410 Hyperbolic Balance Laws in Fluid Mechanics: Complexity, Scales, Randomness (CoScaRa), within the project "Approximation Methods for Statistical Conservation Laws of Hyperbolically Dominated Flow" under Project No. 526024901.

---

[1] A. A. Townsend, *The Structure of Turbulent Shear Flow*, 2nd ed. (Cambridge University Press, Cambridge, New York, 1976).

[2] W. K. George, *The Self-Preservation of Turbulent Flows and Its Relation to Initial Conditions and Coherent Structures*, Advances in Turbulence (Hemisphere, New York, 1989).

[3] I. Wygnanski and H. Fiedler, Some measurements in the self-preserving jet, J. Fluid Mech. **38**, 577 (1969).

[4] N. R. Panchapakesan and J. L. Lumley, Turbulence measurements in axisymmetric jets of air and helium. Part 1. Air jet, J. Fluid Mech. **246**, 197 (1993).

[5] H. J. Hussein, S. P. Capp, and W. K. George, Velocity measurements in a high-Reynolds-number, momentum-conserving, axisymmetric, turbulent jet, J. Fluid Mech. **258**, 31 (1994).

[6] G. G. Xu and R. A. Antonia, Effect of different initial conditions on a turbulent round free jet, Exp. Fluids **33**, 677 (2002).

[7] E. Ferdman, M. V. Otugen, and S. Kim, Effect of initial velocity profile on the development of round jets, J. Propul. Power **16**, 676 (2000).

[8] A. Darisse, J. Lemay, and A. Benaïssa, Budgets of turbulent kinetic energy, Reynolds stresses, variance of temperature fluctuations and turbulent heat fluxes in a round jet, J. Fluid Mech. **774**, 95 (2015).

[9] B. J. Boersma, G. Brethouwer, and F. T. M. Nieuwstadt, A numerical investigation on the effect of the inflow conditions on the self-similar region of a round jet, Phys. Fluids **10**, 899 (1998).

[10] G. N. Taub, H. Lee, S. Balachandar, and S. A. Sherif, A direct numerical simulation study of higher order statistics in a turbulent round jet, Phys. Fluids **25**, 115102 (2013).

[11] C. Bogey and C. Bailly, Large eddy simulations of transitional round jets: Influence of the Reynolds number on flow development and energy dissipation, Phys. Fluids **18**, 065101 (2006).

[12] D. Shin, R. D. Sandberg, and E. S. Richardson, Self-similarity of fluid residence time statistics in a turbulent round jet, J. Fluid Mech. **823**, 1 (2017).

[13] P. F. Fischer, J. W. Lottes, and S. G. Kerkemeier, Nek5000 web page, https://nek5000.mcs.anl.gov/.

[14] A. T. Patera, A spectral element method for fluid dynamics: Laminar flow in a channel expansion, J. Comput. Phys. **54**, 468 (1984).

[15] S. Dong, G. E. Karniadakis, and C. Chryssostomidis, A robust and accurate outflow boundary condition for incompressible flow simulations on severely-truncated unbounded domains, J. Comput. Phys. **261**, 83 (2014).

[16] J. C. R. Hunt, A. A. Wray, and P. Moin, Eddies, streams, and convergence zones in turbulent flows, in *Proceedings of the Summer Program 1988* (Center for Turbulence Research, Stanford, CA, 1988).

[17] P. C. Babu and K. Mahesh, Upstream entrainment in numerical simulations of spatially evolving round jets, Phys. Fluids **16**, 3699 (2004).

[18] C. Bogey and C. Bailly, Turbulence and energy budget in a self-preserving round jet: Direct evaluation using large eddy simulation, J. Fluid Mech. **627**, 129 (2009).

[19] S. Hoyas and J. Jiménez, Reynolds number effects on the Reynolds-stress budgets in turbulent channels, Phys. Fluids **20**, 101511 (2008).

[20] N. N. Mansour, J. Kim, and P. Moin, Reynolds-stress and dissipation-rate budgets in a turbulent channel flow, J. Fluid Mech. **194**, 15 (1988).

[21] S. B. Pope, *Turbulent Flows* (Cambridge University Press, Cambridge, 2000).

[22] E. Motheau and J. Wakefield, On the numerical accuracy in finite–volume methods to accurately capture turbulence in compressible flows, Int. J. Numer. Methods Fluids **93**, 3020 (2021).

[23] V. Saini, H. Xia, and G. Page, Numerical dissipation rate analysis of finite-volume and continuous-Galerkin methods for LES of combustor flow-field, Flow, Turbul. Combust. **111**, 81 (2023).

[24] J. C. Vassilicos, Dissipation in turbulent flows, Annu. Rev. Fluid Mech. **47**, 95 (2015).

[25] C. T. Nguyen and M. Oberlack, DNS data of the turbulent round jet flow at Re = 3500, TUdatalib Repository (Technical University of Darmstadt, 2024), doi:10.48328/tudatalib-1448.

[26] https://www.gauss-centre.eu.

[27] https://www.lrz.de.

[28] S. Rezaeiravesh, R. Vinuesa, and P. Schlatter, A statistics toolbox for turbulent pipe flow in Nek5000, Technical Report TRITA-SCI-RAP 2019008 (KTH Royal Institute of Technology, Sweden, 2019).